Evolution of bubble size distribution, number density, and shape in semi-batch vertical gas-liquid Taylor vortex flow

Mahdi Ramezani[a], Arya Haghighat[a], Meesha J. Legg[b], R. Dennis Vigil[b], Michael G. Olsen[a]

[a] Department of Mechanical Engineering, Iowa State University, Ames, IA, USA

[b] Department of Chemical and Biological Engineering, Iowa State University, Ames, IA, USA

Abstract

Bubble size distribution and bubble ellipticity were measured as a function of axial position in a vertically oriented semi-batch gas-liquid Taylor vortex reactor with varying gas flow rate and inner cylinder rotation speed producing axial Reynolds numbers in the range 23.8-119 and azimuthal Reynolds numbers up to 4.2×10^4. The mean bubble size increases monotonically with axial distance from the bottom of the reactor at the location of gas injection. The functional form of the growth of the mean bubble size with axial position depends upon the azimuthal Reynolds number. Specifically, when the azimuthal Reynolds number is less than 1.3×10^4, the mean bubble size increases linearly with axial distance from the bubble injection point. In contrast, for azimuthal Reynolds numbers greater than this critical value, the mean bubble size increases with axial distance in a sigmoidal manner.

1 Introduction

Examples of bubbly gas-liquid flows in industrial processes are ubiquitous. For example, stirred tanks find numerous applications for waste water treatment [1-3], and bubble columns are commonly used in the chemical process industries for gas-liquid reactions, for mass transfer operations, and for manufacture of synthetic fuels [4,5]. Taylor vortex reactors have also been investigated for their potential to efficiently carry out multi-fluid contacting operations including for water purification [6] and emulsion polymerization [7-8]. Some aspects of the fluid flow for these applications have been investigated including the characterization of flow patterns and regimes [9-13] as well as computational modeling of drag coefficients and pressure loss [14-17]. Experimental characterization of single bubble shape and rise velocity [18,19], bubble breakup

and coalescence [20], and bubble size distribution [21] and growth [22] have also been subjects of previous studies.

Here we consider semi-batch (continuous gas flow, no liquid feed) bubbly Taylor-Couette flow in a vertically oriented reactor, which has applications for cultivation of microalgae [23-25] and gas-liquid absorption [26]. Some aspects of semi-batch vertical gas-liquid Taylor-Couette flow have been investigated previously. These earlier reports have mainly focused on a drastic drag reduction that occurs compared to single phase systems when even a very small volume fraction of gas bubbles is present [27,28] - a result that may aid in machine efficiency. Interphase mass transfer in a vertical semi-batch Taylor vortex reactor has also been the subject of both experimental and computational investigations [29-31].

In most previous investigations of semi-batch bubbly Taylor vortex flow, it has been assumed that gas bubble size does not vary axially. Such an assumption may be justified under circumstances in which bubble-bubble interactions, such as coalescence and breakage, are negligible. However, previous investigations have also demonstrated that bubbles are concentrated radially near the rotating inner cylinder surface, thereby providing greater opportunity for bubble-bubble collision and coalescence events than would be expected if the bubbles were more uniformly distributed radially.

Here we describe experiments using photographic methods to acquire bubble size distributions as a function of downstream axial position from the gas injection location, and it is demonstrated that the mean bubble size increases monotonically with gas flow rate, the rotation speed of the inner cylinder, and the axial location of the bubble. Furthermore, the increase in the mean bubble size with axial position undergoes a transition from a linear dependence to a sigmoidal form as the inner cylinder rotation speed increases beyond a critical value, suggesting a transition in the flow dynamics, and we discuss a possible physical mechanism for the transition between these two regimes.

2 Experimental Setup

The reactor, gas controllers, and motor used in this study were identical to the ones used in previous mass transfer studies, described in detail in Ramezani *et al.* [31] as shown in **Error! Reference source not found.**. The rotating stainless-steel inner shaft has a radius of 3.81 cm. The inner radius of the stationary concentric acrylic outer cylinder is 5.08 cm, corresponding to an annular gap width of 1.27 cm and a radius ratio of $\eta = 0.7$. The outer cylinder height measures 50.8 cm and therefore the length to gap aspect ratio is $\Gamma = 40$. Simulated air (79% nitrogen and 21% oxygen by volume) was mixed using oxygen and nitrogen tanks and was fed at the bottom of the reactor through four evenly spaced sparge stones having a mean pore diameter of 40

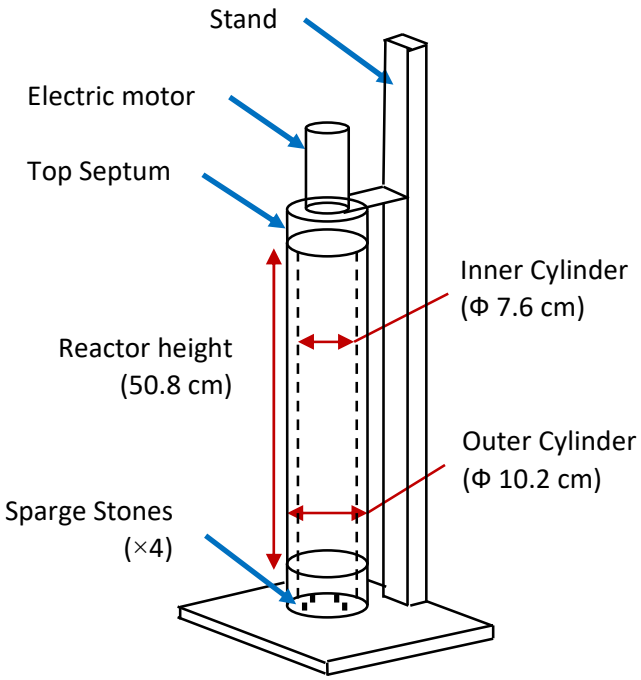

Fig. 1. Depiction of Taylor-Couette vortex reactor showing main dimensions (Ramezani *et al*. 2015).

microns.

The annular gap was filled with 1500 mL of room-temperature deionized water. Experiments were performed at different combinations of shaft rotation speeds and gas flow rates in order to collect bubble size data using photographic methods described below. The electric motor rotated the inner cylinder at speeds ranging from 0 to 800 rpm. The fluid flow can be characterized by azimuthal and axial Reynolds numbers, the former of which is defined as:

$$\mathrm{Re}_\theta = \frac{r_i \omega_i (r_o - r_i)}{\nu_L} \quad (1)$$

Simulated air was fed to the reactor at gas flow rates ranging from 200 to 1000 sccm, and the resulting axial Reynolds number was calculated using the superficial gas velocity and annular gap width as characteristic velocity and length scales, as well as the kinematic viscosity of the liquid phase:

$$\mathrm{Re}_a = \frac{2 u_G (r_o - r_i)}{\nu_L} \quad (2)$$

3 Experimental Methodology

Bubble sizes were measured using a photographic method identical to the one used in a previous study on the effects of surfactant on bubble size and gas-liquid interphase mass transfer [32]. In this method, bubbles were photographed using a DSLR camera (EOS Rebel T3i) fitted with an 18-55mm zoom lens. An external double indirect flash illumination setup was used to minimize reflected light entering the camera lens [32]. A flash sync speed of 1/200 s was found to be adequate for freezing the bubble motion and this shutter speed was used with an aperture setting of f/10 to capture all in-situ bubble images. A sample photograph of the bubbles is shown in Fig. 2. Multiple photos were taken for each specific combination of rotation speed and gas flow rate, thereby providing more than 30 instantaneous bubbly flow measurement photographs for each combination. Major and minor axes for each bubble, as well as the axial location of each bubble were measured and recorded for a sufficient number of images so that approximately one thousand unique bubble measurements were performed at each combination of cylinder rotation speed and gas flow rate.

Following the discussions in Ramezani *et al*. [32], Eq. 3 was used for calculation of the Sauter diameter for individual bubbles (and for subsequent statistical analysis) based upon the experimental observation that the bubbles are prolate ellipsoids and where *l* and *m* represent the major and minor axes, respectively.

$$d_{b,s}^{\text{prolate}} = d_s = \sqrt{{}^1\!/_2 \left(m^2 + {}^{lm}\!/_E \sin^{-1} E \right)} \quad (3)$$

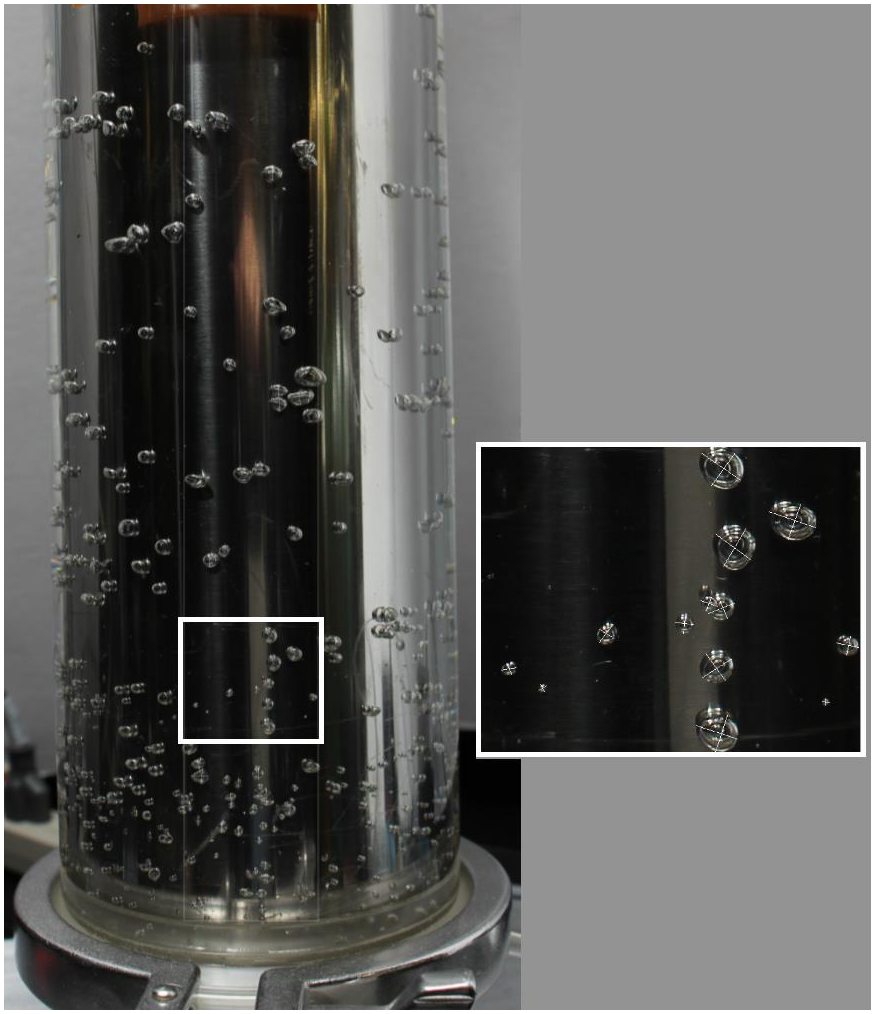

Fig. 2 Sample bubble image at inner cylinder rotation speed of 300 rpm and 200 sccm. The inset shows chords overlaid on bubbles used to determine bubble size.

The ellipticity of the bubbles (E) is defined in Eq. 4, which produces a value of 0 for perfect spheres and 1 for line segments.

$$E = \sqrt{1 - \frac{m^2}{l^2}} \tag{4}$$

4 Results and Discussion

Representative bubble diameter distributions at three axial locations using uniform bin sizes are shown in Fig. 3 for fixed gas flow rate and cylinder rotation speed. Corresponding log-normal distributions are also plotted in this figure using the experimentally-determined values for the

bubble diameter mean and standard deviation. The plots demonstrate that the bubble Sauter diameter distributions at each axial location are well represented by log-normal probability distribution functions. Figure 3 also shows that the mean bubble diameter increases significantly with increasing axial distance from the reactor inlet.

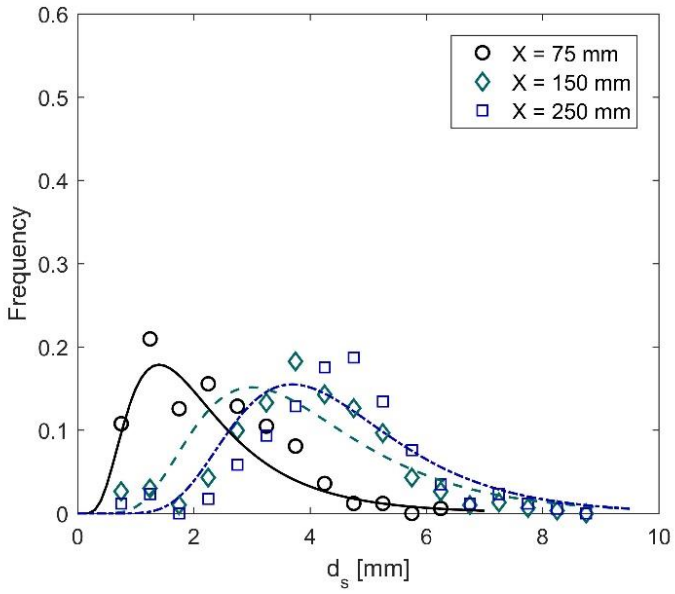

Fig. 3 Probability distribution function of bubble diameter at different axial locations at 600 rpm rotation speed and 200 sccm gas flow rate.

Since the bubble size distribution was determined to be a function of axial location, a moving average window (333 bubbles) was used for calculations of the bubble size, shape, and number density statistics. Figure 4 shows measured bubble diameters for two sample cases with rotation speeds and gas flow rates of 200 rpm ($Re_\theta = 1.0\times10^4$) and 600 sccm ($Re_a = 71.6$), and 600 rpm ($Re_\theta = 3.0\times10^4$) and 200 sccm ($Re_a = 23.9$), respectively. The values of the bubble diameter nearest to the reactor inlet and outlet are defined as the mean of the first 249 and last 203 measured bubble diameters corresponding on average to axial locations of $X_{in} = 52$ mm and $X_{out} = 233$ mm, respectively. Markers represent the diameters of individually measured bubbles. The solid lines represent moving averages of the bubble diameter, and the dotted lines show the corresponding 95% confidence intervals assuming a log-normal bubble size distribution. In all experiments considered here, the mean bubble diameter was found to increase monotonically with downstream axial position. The bubble number density, which is inversely proportional to the bubble diameter, is also shown in the same figure (dashed line).

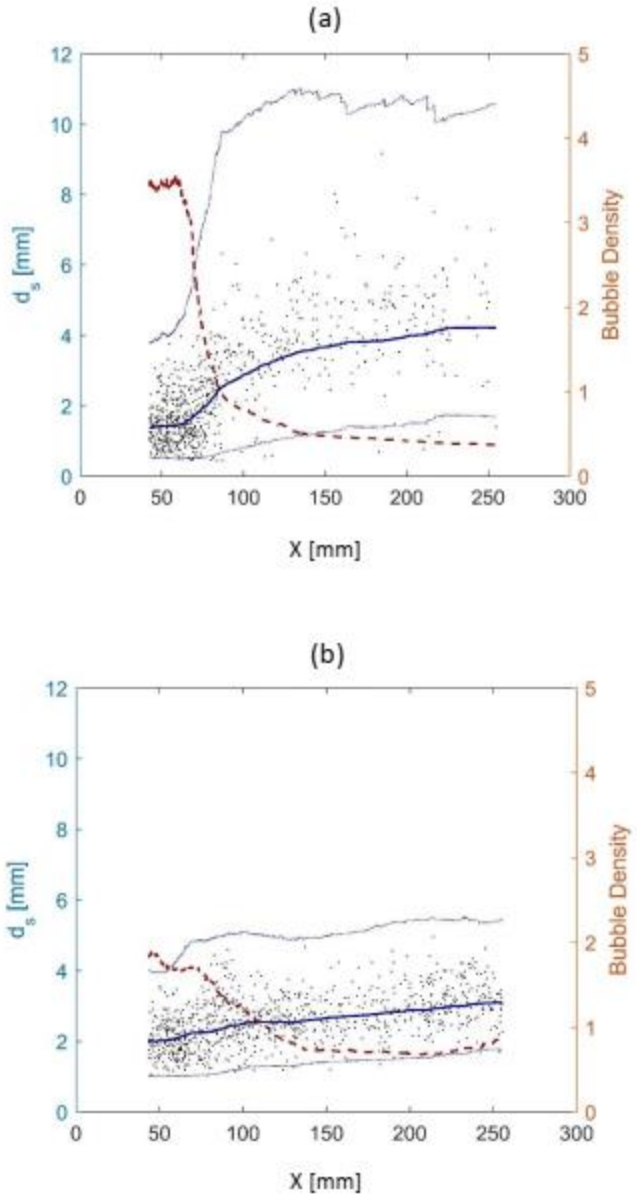

Fig. 4 (a) Measured bubble diameters at 200 rpm rotation speed and 600 sccm gas flow rate, and (b) measured bubble diameters at 600 rpm rotation speed and 200 sccm gas flow rate. Markers: individual bubble diameter. Solid line: moving average. Dotted line: 95% confidence intervals. Dashed line: number density. The first optically accessible axial location is 41 mm from the bottom of the reactor, and thus the plotting of data begins at that location.

As with bubble diameter, the moving average bubble ellipticity increases monotonically with downstream distance from the point of gas injection, as shown for two representative cases plotted in Fig. 5 using rotation speeds and gas flow rates of 200 rpm, 600 sccm ($Re_\theta = 1.03\times10^4$, $Re_a = 71.5$) and 600 rpm, 200 sccm ($Re_\theta = 3.10\times10^4$, $Re_a = 23.8$). Normalized histograms of bubble ellipticity for the entire reactor volume are also shown, and these demonstrate that bubbles are strongly non-spherical.

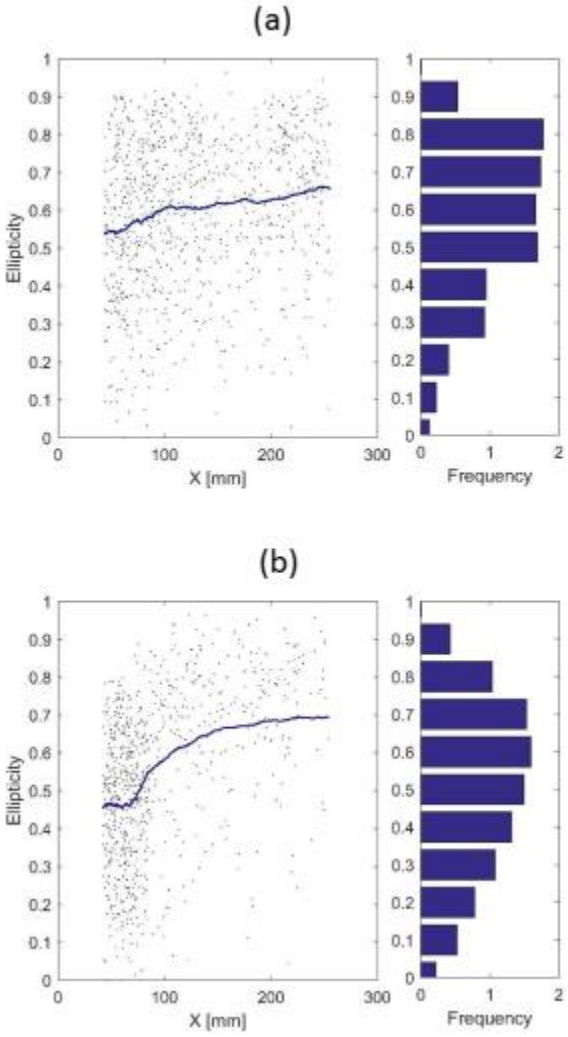

Fig. 5 (a) Measured bubble ellipticity at 200 rpm rotation speed and 600 sccm gas flow rate ($Re_\theta = 1.03\times10^4$, $Re_a = 71.5$), and (b) measured bubble ellipticity at 600 rpm rotation speed and 200 sccm gas flow rate ($Re_\theta = 3.10\times10^4$, $Re_a = 23.8$).

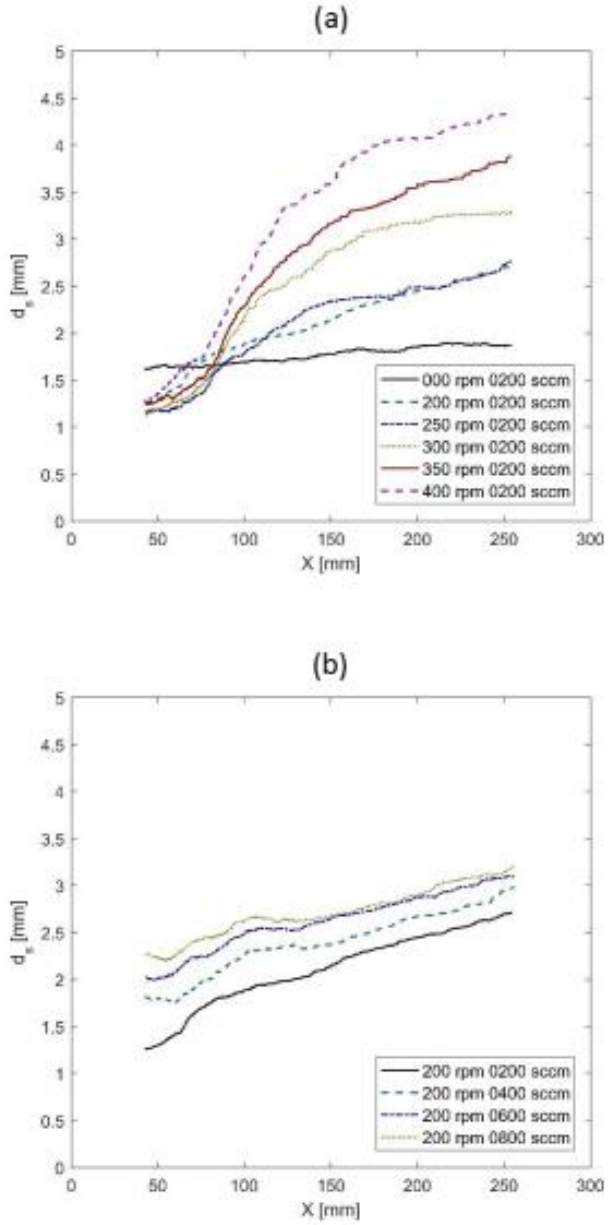

Fig. 6 Moving average of bubble diameters showing the effect of inner cylinder rotation speed and gas flow rate: (a) fixed gas flow rate (200 sccm) for various inner cylinder rotation speeds, and (b) fixed rotation speed (200 rpm) for various gas flow rates.

The effects of inner cylinder rotation speed and gas flow rate on axial bubble size evolution are depicted in Fig. 6. Specifically, Fig. 6 (a) shows axial bubble diameter profiles for fixed gas flow rate (200 sccm) using various inner cylinder rotational speeds. The bubble diameter at the most upstream observation point appears to be relatively insensitive to cylinder rotation speed except when there is no cylinder rotation at all, in which case bubbles near the point of injection are

significantly larger than in cases with cylinder rotation. Evidently, the presence of a cross flow driven by the rotating cylinder causes bubbles to (1) detach from sparge stones at a smaller size than in the non-rotating case where there is no cross flow and/or (2) bubble coagulation near sparge stones is suppressed by the imposition of an azimuthal velocity component. Figure 6 (a) also shows that for low cylinder rotation speeds the increase in bubble diameter with downstream location is approximately linear, and that this linear relationship begins to transition to a sigmoidal curve at a cylinder speed of approximately 250 rpm (Re_θ = 13,000). For rotation speeds above this value, the sigmoidal character of the growth curve becomes more pronounced, and the bubble diameter at the most downstream location increases with increasing cylinder rotation speed.

Note that the critical azimuthal Reynolds number at which the transition from a linear to a sigmoidal axial bubble size distribution coincides with another transition observed in simulations of vertical semi-batch gas-liquid Taylor vortex flow. Specifically, Gao *et al*. [29] found that the global turbulent kinetic energy dissipation rate starts to increase rapidly with increasing cylinder rotation speed when $Re_\theta \geq$ 9,700. Moreover, these investigators showed that the rapid increase in turbulence dissipation is radially concentrated near the rotating inner cylinder. However, their simulations were performed for a Taylor vortex reactor with different inner and outer cylinder radii as well as radius ratio (η) than those considered here. In order to account for these geometric differences, the Taylor number, defined as

$$\mathrm{Ta} \equiv 4\mathrm{Re}_\theta^2\left[\frac{1-\eta}{1+\eta}\right], \tag{5}$$

should be used as the similarity criterion for reactors with differing geometry. By applying the above equation for the two reactor systems, the critical value of Re_θ reported by Gao *et al*. [29] for onset of rapid increase in turbulent kinetic energy dissipation rate corresponds to a value of Re_θ = 13,200 in the reactor used here. This value is nearly identical to the critical value (13,000), discussed above, for the transition from a linear to sigmoidal axial droplet size distribution. The coincidence of these two critical azimuthal Reynolds numbers supports the inference that the rapid rise in turbulence dissipation rate near the inner cylinder wall as the cylinder rotation speed increases, also promotes bubble coalescence.

Axial bubble size distributions for a fixed rotation speed of 200 rpm (Re_θ = 10,000) and gas flow rates ranging from 200 to 800 sccm (Re_a = 23.9-95.5) are plotted in Fig. 6 (b). At the observation location nearest the point of gas injection, the bubble diameter increases with increasing gas flow rate. In addition, it is evident that the mean bubble diameter grows approximately linearly (with a slope that is apparently not very sensitive to gas flow rate) with downstream position. These observations, taken together, suggest that the primary role of the gas flowrate is that it strongly impacts the size of bubbles as they enter the reactor. Thereafter, it has little effect on downstream bubble growth, which instead is largely governed by the cylinder angular velocity, as is shown in Fig. 6 (a).

The effect of inner cylinder rotation speed and gas flow rate on the ellipticity of bubbles is depicted in Fig. 7. Figure 7 (a) shows that bubble ellipticity generally increases with downstream position for all angular cylinder rotation speeds considered, including the case without cylinder rotation (i.e., an annular bubble column). Figure 7 (b) shows that for a fixed rotation speed, the increase in bubble ellipticity is similar for all of the flow rates investigated, the effect of increasing gas flow rate appears to have the effect of increasing the bubble ellipticity at the furthest upstream observation location. These plots illustrate two other features. First, there exists a non-monotonic dependence of bubble ellipticity on azimuthal Reynolds number. Bubble ellipticity is large in the absence of cylinder rotation, ellipticity is relatively low for the smallest rotation speeds considered, but it increases again as the cylinder speed increases, particularly at locations far downstream from the gas injection location. This non-monotonic behavior echoes the non-monotonic dependence of bubble diameter on cylinder rotation speed near the point of gas injection, as seen in Fig. 8, and therefore it implies a correlation of bubble diameter and ellipticity. It is also worth noting that the nature of the observed non-sphericity also changes as the inner cylinder rotation speed increases. Specifically, in the absence of cylinder rotation, the buoyancy-driven rise of bubbles causes them to take on the shape of oblate spheroids [33], whereas the imposition of an azimuthal flow leads to prolate stretching [31].

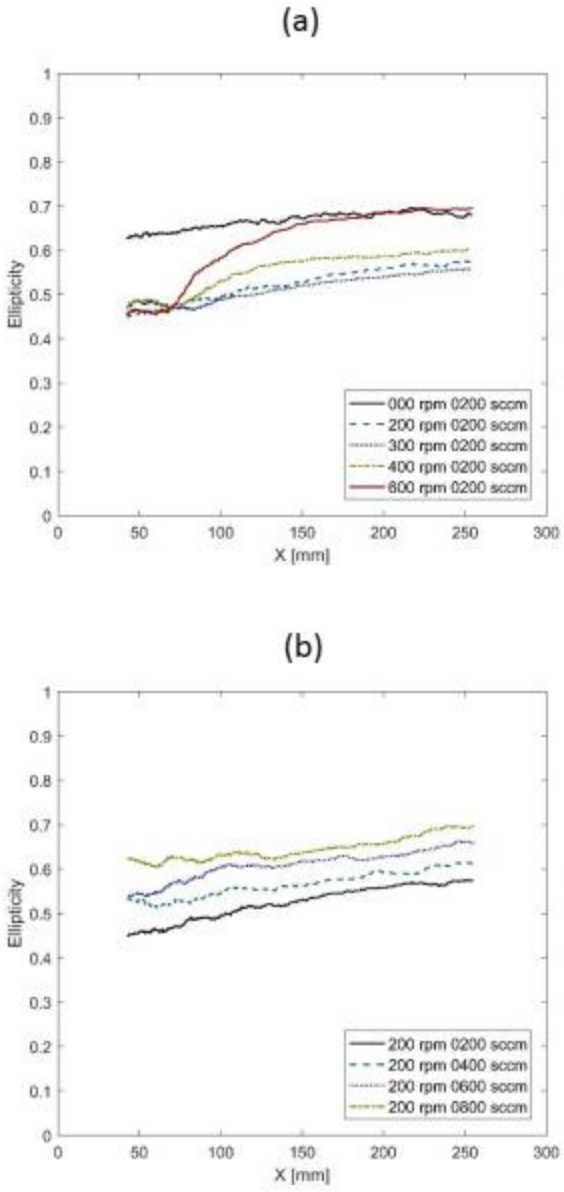

Fig. 7 Moving average of bubble ellipticity showing the effect of inner cylinder rotation speed and gas flow rate: (a) fixed gas flow rate (200 sccm) for various inner cylinder rotation speeds, and (b) fixed rotation speed (200 rpm) for various gas flow rates.

A second striking feature of Fig. 7 (a) is the fact that the axial ellipticity profiles largely mirror the shapes of the corresponding axial profiles for mean diameter shown in Fig. 6 (a) insofar as they exhibit a linear to sigmoidal axial profile transition with increasing azimuthal Reynolds number. However, the critical value for azimuthal Reynolds number in this case is approximately 20,800. These observations suggest that there is a linear relationship between bubble diameter

and ellipticity, which can be understood as a direct consequence of droplet deformation in a shear field.

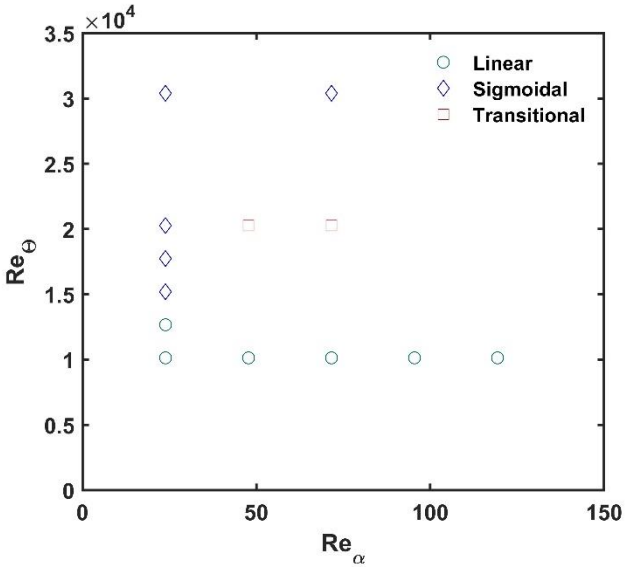

Fig. 8. Regime map showing transition boundaries for bubble diameter axial profile shapes. Diamonds represent sigmoidal growth and circles represent linear growth.

A regime map showing the combined effects of rotation speed (Re_θ) and gas flow rate (Re_a) on the shapes of the axial bubble diameter profiles is plotted in Fig. 8, where circles and diamonds represent linear and sigmoid-shaped growth curves, respectively. The shaded diamonds in this figure signify a few transition cases that are intermediate between the linear and sigmoidal growth regimes and therefore are not well-characterized by either a linear or a sigmoidal function.

Conclusions

Optical experiments were performed in order to quantify the axial distribution of gas bubble size and shape when air is sparged continuously into a vertically oriented Taylor vortex flow device containing water. Two operating parameters corresponding to radial and axial Reynolds numbers (inner cylinder angular velocity and sparged gas volumetric flow rate) were varied in order to

determine the effects of the azimuthal and axial Reynolds numbers on gas bubble size and ellipticity.

Based upon these experiments, it was shown that the feed gas flow rate (axial Reynolds number) has little impact on axial bubble growth, but that it does strongly influence the size of the bubbles entering the reactor. In contrast, the inner cylinder rotation speed (azimuthal Reynolds number) has a secondary impact on the entering bubble size but it strongly impacts the axial growth rate of bubbles. In all cases considered, and at any axial location in the reactor, a log-normal distribution of Sauter bubble diameter was obtained.

Experiments also revealed that for rotation speeds less than 200 rpm ($Re_\theta=1.03\times10^4$) bubble size increases linearly with axial position; however, for rotation speeds greater than 250 rpm, this dependency transitions to a sigmoidal shape. This onset of change was shown to correspond to a Taylor number of ~13,000 which is nearly identical to the threshold for a rapid increase in turbulent kinetic energy dissipation rate based on available numerical simulations in the literature. This transition from linear to sigmoidal behavior has been depicted using a regime map.

Finally, experiments showed that ellipticity of the bubbles increases with downstream axial position from the point of gas injection in the reactor, and the evolution of ellipticity with downstream location mirrors the bubble size growth curve. It was attempted to find a correlation between the size and shape of the bubbles but the collected data suggests no direct correlation between bubble diameter and ellipticity.

Acknowledgments

The authors thank Dr. Xi Gao and Dr. Bo Kong for helpful discussions. Financial support was provided for this work by National Science Foundation Grant CBET-1236676.

References

1. Kapek A, Heindel TJ. Correlating gas-liquid mass transfer in a stirred-tank reactor. Chem Eng Res Des. 2006 84:239-245.

2. Gargouri B, Karray F, Mhiri N, Aloui F, Sayadi S. Application of a stirred tank bioreactor (CSTR) for bioremdiation of hydrocarbon-rich industrial wastewater effluents. J Hazard Mater. 2011 189:427-434.

3. Labík L, Vostal R, Moucha T, Rejl F, Kordac M. Volumetric mass transfer coefficient in multiple-impeller gas-liquid contactors. Scaling-up study for various impeller types. Chem Eng J 2014 240:55–61.

4. Kantarci N, Borak F, Ulgen KO. Bubble column reactors. Process Biochem. 2005 40:2263–2283.

5. Behkish A, Lemoine R, Sehabiague L, Oukaci R, Morsi B. Gas holdup and bubble size behavior in a large-scale slurry bubble column reactor operating with an organic liquid under elevated pressures and temperatures. Chem Eng J 2007 128:69–84.

6. Mittal S, Tezduyar TE. Comment on "Experimental investigation of Taylor vortex photocatalytic reactor for water purification." Chem. Eng. Sci. 2017 192:1262.

7. Kataoka K, Ohmura N, Kouzu M, Simamura Y, Okubo M. Emulsion polymerization of styrene in a continuous Taylor vortex flow reactor. Chem Eng Sci 1995 50:1409–1416.

8. Wei X, Takahashi H, Sato S, Nomura M. Continuous emulsion polymerization of styrene in a single Couette-Taylor vortex flow reactor. J Appl Polym Sci 2001 80:1931–1942.

9. Kaichiro M, Ishii M. Flow regime transition criteria for upward two-phase flow in vertical tubes. Int J Heat Mass Transf 1984 27:723–737.

10. Dukler AE, Taitel Y. Flow pattern transitions in gas-liquid systems: measurement and modeling. Multiph Sci Technol 1986 2:1–94.

11. Mishima K, Hibiki T. Some characteristics of air-water two-phase flow in small diameter vertical tubes. Int J Multiph Flow 1996 22:703–712.

12. Ishii M, Zuber N. Drag coefficient and relative velocity in bubbly, droplet or particulate

flows. AIChE J 1979 25:843–855.

13. Mishima K, Hibiki T, Nishihara H. Some characteristics of gas-liquid flow in narrow rectangular ducts. Int J Multiph Flow 1993 19:115–124.

14. Ishii M, Mishima K. Two-fluid model and hydrodynamic constitutive relations. Nucl Eng Des 1984 82:107–126.

15. Hibiki T, Ishii M. One-dimensional drift-flux model and constitutive equations for relative motion between phases in various two-phase flow regimes. Int J Heat Mass Transf 2003 46:4935–4948.

16. Dong S. Direct numerical simulation of turbulent Taylor–Couette flow. J Fluid Mech 2007 587:373–393.

17. Pirrò D, Quadrio M. Direct numerical simulation of turbulent Taylor-Couette flow. Eur J Mech B/Fluids 2008 27:552–566.

18. Grace JR, Harrison D. The influence of bubble shape on the rising velocities of large bubbles. Chem Eng Sci 1967 22:1337–1347.

19. Grace JR, Harrison D. The behaviour of freely bubbling fluidised beds. Chem Eng Sci 1969 24:497–508.

20. Crabtree JR, Bridgwater J. Bubble coalescence in viscous liquids. Chem Eng Sci 1971 26:839–851.

21. Rodrigues RT, Rubio J. New basis for measuring the size distribution of bubbles. Miner Eng 2003 16:757–765. https://doi.org/10.1016/S0892-6875(03)00181-X

22. Mori S, Wen CY. Estimation of bubble diameter in gaseous fluidized beds. AIChE J 1975 21:109–115.

23. Miller RL, Fredrickson AG, Brown AH, Tsuchiya HM. Hydromechanical method to increase efficiency of algal photosynthesis. Ind Eng Chem Process Des Dev 1964 3:134–143.

24. Kong B, Vigil RD. Light-limited continuous culture of Chlorella vulgaris in a Taylor vortex reactor. Environ Prog Sustain Energy 2013 32:884–890.

25. Kong B, Vigil RD. Simulation of photosynthetically active radiation distribution in algal photobioreactors using a multidimensional spectral radiation model. Bioresour Technol 2014 158:141–148.

26. Yue J, Chen G, Yuan Q, Luo L, Gonthier Y. Hydrodynamics and mass transfer characteristics in gas-liquid flow through a rectangular microchannel. Chem Eng Sci 2007 62:2096–2108.

27. Van Gils DPM, Huisman SG, Bruggert GW, Sun C, Lohse D. Torque scaling in turbulent Taylor-Couette flow with co- and counterrotating cylinders. Phys Rev Lett 2011 106:024502

28. Maryami R, Farahat S, Poor MJ, Mayam MHS. Bubbly drag reduction in a vertical Couette-Taylor system with superimposed axial flow. Fluid Dyn Res 2014 46:055504

29. Gao X, Kong B, Ramezani M, Olsen MG, Vigil RD. An adaptive model for gas-liquid mass transfer in a Taylor vortex reactor. Int J Heat Mass Transf 2015 91:433–445.

30. Gao X, Kong B, Vigil RD. CFD investigation of bubble effects on Taylor-Couette flow patterns in the weakly turbulent vortex regime. Chem Eng J 2015 270:508–518.

31. Ramezani M, Kong B, Gao X, Olsen MG, Vigil RD. Experimental measurement of oxygen mass transfer and bubble size distribution in an air-water multiphase Taylor-Couette vortex bioreactor. Chem Eng J. 2015 279:286-296.

32. Ramezani M, Legg MJ, Haghighat A, Li Z, Vigil RD, Olsen MG. Experimental investigation of the effect of ethyl alcohol surfactant on oxygen mass transfer and bubble size distribution in an air-water multiphase Taylor-Couette vortex bioreactor. Chem Eng J 2017 319:288–296.

33. Polli M, Stanislao M Di, Bagatin R, Abu Bakr, E, Masi, M. Bubble size distribution in the sparger region of bubble columns. Chem Eng Sci. 2002 57:197–205.